Korean Journal of Remote Sensing, Vol.25, No.3, 2009, pp.243~253

Wind Retrieval from X-band SAR Image Using Numerical Ocean Scattering Model

Duk-jin Kim †

School of Earth and Environmental Sciences, Seoul National University

Abstract : For the last 14 years, space-borne satellite SAR system such as RADARSAT-1, ERS-2, and ENVISAT ASAR have provided a continuous observation over the ocean. However, the data acquired from those systems were limited to C-band frequency until the advent of the first spaceborne German X-band SAR system TerraSAR-X in 2007. Korea is also planning to launch the nation's first X-band SAR satellite (KOMPSAT-5) in 2010. It is timely and necessary to develop X-band models for estimating geophysical parameters from these X-band SAR systems. In this study, X-band wind retrieval model was investigated and developed based on numerical ocean scattering model (radar backscattering model and hydrodynamic interaction model). Although these models have not yet been tested and validated for broad ranges of wind conditions, the estimated wind speeds from TerraSAR-X data show generally good agreement with in-situ measurements.

Key Words : X-band, wind retrieval, numerical model, TerraSAR-X.

1. Introduction

The availability of civilian space-borne SAR systems operating in three frequencies (X-, C-, and L-band) simultaneously become a reality for the first time in history as COSMO-SkyMed and TerraSAR-X were in orbit in June 2007. Currently many civilian SAR satellites such as ERS-2 (ESA, C-band), RADARSAT-1 (CSA, C-band), ENVISAT (ESA, C-band), ALOS (JAXA, L-band), COSMO-SkyMed (ASI, X-band), TerraSAR-X (DLR, X-band), and RADARSAT-2 (CSA, C-band) are operating and transmitting Earth observation data to the ground. As more SAR satellites are in orbit to cover the whole globe at least once a day, the SAR system is positioning itself as one of the most powerful tools for real-time monitoring, in particular over the ocean. The SAR system can observe the Earth's surface with very high resolution, large spatial coverage and day and night, which makes it a valuable tool for measuring geophysical parameters such as ocean surface winds, waves and currents. Although space-based scatterometers have provided global wind information for a wide range of applications, the relatively low spatial resolution of the scatterometer (25 km × 25 km) made it difficult to observe wind field in coastal regions and ocean meso-scale structures. The SAR, on the other hand, can generate

Received June 8, 2009; Revised June 29, 2009; Accepted July 1, 2009.

† Corresponding Author: Duk-jin Kim (djkim@snu.ac.kr)

high-resolution wind filed. The high-resolution wind field can be valuable and be used in many area of applications such as local forecasting, typhoon monitoring, coastal engineering, energy production (wind turbine installation), ship navigation, and so on.

Sea surface wind is a critical parameter to interpret SAR images because the dominant scattering mechanism is Bragg scattering at moderate angles of incidence - as the wind speed increases, the height of waves at the Bragg wavelength increases (Valenzuela, 1978). Most methods for extracting wind vectors from SAR data use a geophysical model function (GMF) such as the CMOD (C-band model function) series in combination with wind directions derived from wind aligned signatures in the SAR image or from the external source of the wind direction to estimate wind speed (Hersbach *et al.*, 2007; Stoffelen and Anderson, 1997). But the CMOD series wind GMF is only applicable to C-band VV-polarization radar data (e.g., ERS, ENVISAT and RADARSAT). Recently, several new X-band SAR systems have been developed and put into orbit. Currently, COSMO-SkyMed and TerraSAR-X launched in 2007 are in operation, and KOMPSAT-5 and TanDEM-X are in preparation to be launched soon. It is thus timely and necessary to develop X-band GMF for estimating wind field from the emerging X-band SAR satellites. There have been several attempts to investigate the characteristics of X-band ocean backscattering (Lehner *et al.*, 2007; Masuko *et al.*, 1986; Thompson *et al.*, 2008). In this study, a new X-band wind retrieval model was investigated by combining theoretical ocean scattering models - radar backscattering model and a hydrodynamic interaction model, with SAR measurements.

2. Numerical models for ocean SAR simulation

1) Radar backscattering model

The radar backscattering from the ocean surface can be calculated using the two-scale model or composite surface model (Romeiser *et al.*, 1997; Wright, 1968). These models were based on resonant Bragg scattering theory, and the normalized radar cross section (NRCS, σ^0) of a slightly tilted surface of the ocean is proportional to the wave height spectral density of the Bragg waves which are in resonance with the electromagnetic waves. The tilted Bragg contribution to the NRCS can be written as an integral over the surface slopes (Lyzenga and Bennett, 1988),

$$\sigma_B^0(\theta,\phi) = 8\pi k_0^4 \iint |G(\theta,\eta_x,\eta_y)|^2 \cdot \Psi(2k_0 \sin\theta',\phi) \, p(\eta_x,\eta_y) d\eta_x d\eta_y \quad (1)$$

where θ is the incidence angle, ϕ is the radar look direction, k_0 is the electromagnetic wave number, η_x and η_y are the surface slope in the plane of incidence and in the orthogonal direction, respectively. $G(\theta, \eta_x, \eta_y)$ is a scattering coefficient which depends on polarization, $\Psi(k, \phi)$ is the surface wave spectral density, and $p(\eta_x, \eta_y)$ is the large-scale slope probability density function. The scattering coefficients for vertical (VV) and horizontal (HH) polarization can be given by (Wright, 1968),

$$G_{vv}(\theta,\eta_x,\eta_y) = \frac{(\varepsilon-1)[\varepsilon(1+\sin^2\theta')-\sin^2\theta']}{[\varepsilon\cos\theta+\sqrt{\varepsilon-\sin^2\theta'}]^2}\cos^2\theta' \quad (2)$$

$$G_{HH}(\theta,\eta_x,\eta_y) = \frac{(\varepsilon-1)\cos^2\theta'}{[\cos\theta+\sqrt{\varepsilon-\sin^2\theta'}]^2} + G_{vv}\frac{\eta_y^2}{\sin^2\theta'} \quad (3)$$

where ε is the dielectric constant of the sea water and $\theta' = \theta + \tan^{-1}\eta_x$ is the local incidence angle for a long ocean wave having a slope η_x in the plane of incidence.

The total NRCS, in addition to tilted Bragg

contribution of Eq. (1), can be obtained by adding the physical optics or specular contribution,

$$\sigma_s^0(\theta,\phi) = \frac{\pi}{\cos^4\theta}|R(0)|^2 p(\tan\theta, 0) \quad (4)$$

where $R(0) = \frac{1-\varepsilon}{1+\varepsilon}$ is the Fresnel reflection coefficient for normal incidence.

For the calculation of the large-scale slope probability density function, $p(\eta_x, \eta_y)$, the tilt angles of the large-scale facets were assumed to be Gaussian distribution and zero mean slopes. The surface wave spectral density, $\Psi(k, \phi)$ in Eq. (1) was calculated from the hydrodynamic interaction model with various wind speed conditions described in the next section.

2) Hydrodynamic interaction and ocean wave spectrum models

In general, if there is ambient current, the surface wave spectral density (Ψ) can be modelled by the hydrodynamic interaction model that can solve the high-wavenumber portion of the wind-wave by the action balance equation (Komen, 1994),

$$\frac{\partial N}{\partial t} + (U + C_g)\frac{\partial N}{\partial x} - \left(k\frac{\partial U}{\partial x}\right)\frac{\partial N}{\partial k} = Q(k,x,t) \quad (5)$$

where N is the action spectral density, C_g is the group velocity, U is the surface current, and x and k is the spatial position and wave-number of the surface waves, respectively. The quantity Q on the right-hand side of the equation is the net source function which accounts for wind input and wave energy dissipation (Hughes, 1978; Thompson and Gasparovic, 1986):

$$Q = \mu N\left(1 - \frac{N}{N_0}\right) \quad (6)$$

where μ is a wave relaxation rate and N_0 is the equilibrium action spectral density. For the calculation of μ, the growth parameter suggested by Plant (Plant, 1982) was used,

$$\mu = 0.043\left(\frac{u_*}{c}\right)^2 \omega\,|\cos(\phi - \phi_w)| \quad (7)$$

where u_* denotes the friction velocity, $c = \omega/k$ is the phase velocity, and ϕ_w is the wind direction. The relationship between the action spectral density (N) and the surface wave spectral density (Ψ) is given by (Phillips, 1977)

$$N(k,\phi) = \rho\frac{\omega}{k}\Psi(k,\phi) \quad (8)$$

where ω is the intrinsic wave frequency, which is given by

$$\omega = \sqrt{gk + \frac{\tau}{\rho}k^3} \quad (9)$$

where g is the gravitational acceleration, τ is the surface tension, and ρ is the density of water.

In order to solve the Eq. (5) and to calculate the NRCS of ocean surface using the radar backscattering model, the equilibrium ocean wave spectrum (Ψ) should be first determined. There are many ocean wave spectrum models for describing of wind-generated ocean surface waves (Elfouhaily *et al.*, 1997). Among the ocean wave spectrum models that are widely used in microwave radar scattering studies, Romeiser's ocean wave spectrum model was used in this study because it is optimized using a variety of NRCS values measured from airborne scatterometers for different wind speeds, polarizations, incidence angles, and radar frequencies including X-band measurements.

The Romeiser's ocean wave spectrum is expressed as (Romeiser *et al.*, 1997):

$$\Psi(k,\phi,u_{10}) = P_L(k,u_{10})W_H(k)(u_{10})^{\beta(k)}k^{-4}S(k,\phi,u_{10}) \quad (10)$$

where P_L is a factor which describes a low wavenumber roll-off and given by:

$$P_L = 0.00195\exp\left[-\frac{k_p^2}{k^2} + 0.53\exp\left(-\frac{(\sqrt{k}-\sqrt{k_p})^2}{0.32k_p}\right)\right] \quad (11)$$

where $k_p = \frac{1}{\sqrt{2}} \frac{g}{u_{10}^2}$ is the peak wavenumber and u_{10} is the wind speed at a height of 10 m. The β is wind speed exponent and is founded:

$$\beta = \left[1 - \exp\left(-\frac{k^2}{(183\ \text{rad/m})^2}\right)\right]\exp\left(-\frac{k}{3333\ \text{rad/m}}\right) + \left[1 - \exp\left(-\frac{k}{33\ \text{rad/m}}\right)\right]\exp\left[-\left(\frac{k - 140\ \text{rad/m}}{220\ \text{rad/m}}\right)^2\right] \quad (12)$$

The factor W_H in Eq. (10) determines the shape of the high wavenumber region (resonant Bragg wave region) of the spectrum, and is expressed by

$$W_H = \frac{\left(1 + \left(\frac{k}{280\ \text{rad/m}}\right)^{7.2}\right)^{0.5}}{\left(1 + \left(\frac{k}{75\ \text{rad/m}}\right)^{2.2}\right)\left(1 + \left(\frac{k}{1300\ \text{rad/m}}\right)^{3.2}\right)^2} \exp\left(-\frac{k^2}{(8885\ \text{rad/m})^2}\right) \quad (13)$$

Finally, the spreading function S describes the directional behaviour of the spectrum, which is defined by

$$S = \exp\left(-\frac{\phi^2}{2\delta^2}\right) \quad (14)$$

where

$$\frac{1}{2\delta^2} = 0.14 + 0.5\left(1 - \exp\left(-\frac{ku_{10}}{400\ \text{rad/m}}\right)\right) + 5\exp(2.5 - 2.6\ln(u_{10}) - 1.3\ln(k)) \quad (15)$$

The resulting ocean wave spectrum (curvature spectrum; $k^4\Psi$) calculated using the Eqs. (10)-(14) is shown in Fig. 1 as a function of wave-numbers for wind speeds of 5, 10, 15, and 20 m/s, respectively. The secondary gravity-capillary peaks were observed at wavenumbers between 100 and 300 rad/m, and the depression which can be the unique feature of the Romeiser's spectrum occurred between 300 and 600 rad/m.

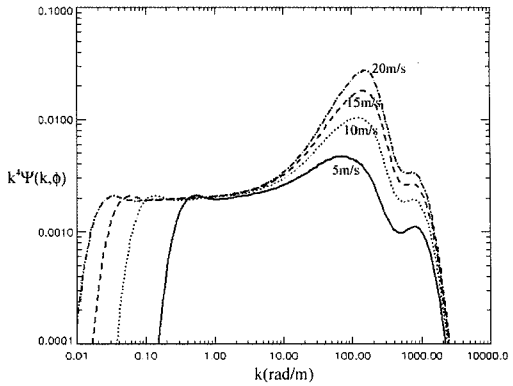

Fig. 1. Romeiser's (curvature) ocean wave spectrum at ϕ = 0 for wind speeds of 5, 10, 15, and 20 m/s, respectively.

3) Numerical model simulation results

For NRCS calculations, numerical simulations were made at C-band (5.3 GHz) as well as at X-band (9.65 GHz) in both VV and HH-polarization for incidence angles from 20° to 60°, wind speed values ranging from 2 to 30 m/s and wind direction ranging from 0 to 360°. The ambient current for the numerical calculation in this study was assumed as 0 m/s.

In order to test the performance of the numerical model simulation, the C-band NRCS values calculated from the radar backscattering model and the Romeiser's ocean wave spectrum were compared with the CMOD4 model function (Fig. 2). The

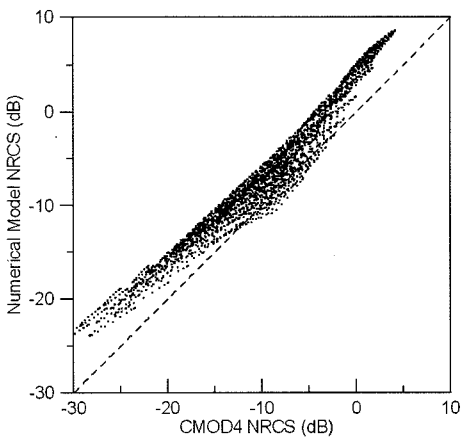

Fig. 2. Relationship between NRCSs from CMOD4 model function and from the numerical model simulation.

CMOD4 model function can provide us the relation between the NRCS and surface wind speed. The CMOD4 model was originally derived empirically from a large number of C-band, VV-polarization NRCS measurements made by the ERS-1 scatterometer over an incidence angle range from 18° to 57° and a wind speed range from about 0-20 m/s (Stoffelen and Anderson, 1997). Although the C-band NRCSs simulated from numerical models are somewhat higher than the results of CMOD4 model function, they are linearly related. It represents that the radar backscattering model and hydrodynamic interaction model reasonably well predict the values of NRCS at given incidence angles, wind speed, and wind direction ranges.

The X-band NRCSs for the same ranges of incidence angle, wind speed, and wind direction were also simulated using the models and the results are shown in Fig. 3. The simulated data of X-band showed the explicit dependence on both wind speed and wind direction (Fig. 3) as the CMOD4 model function does (Fig. 4). Note that the X-band NRCS is

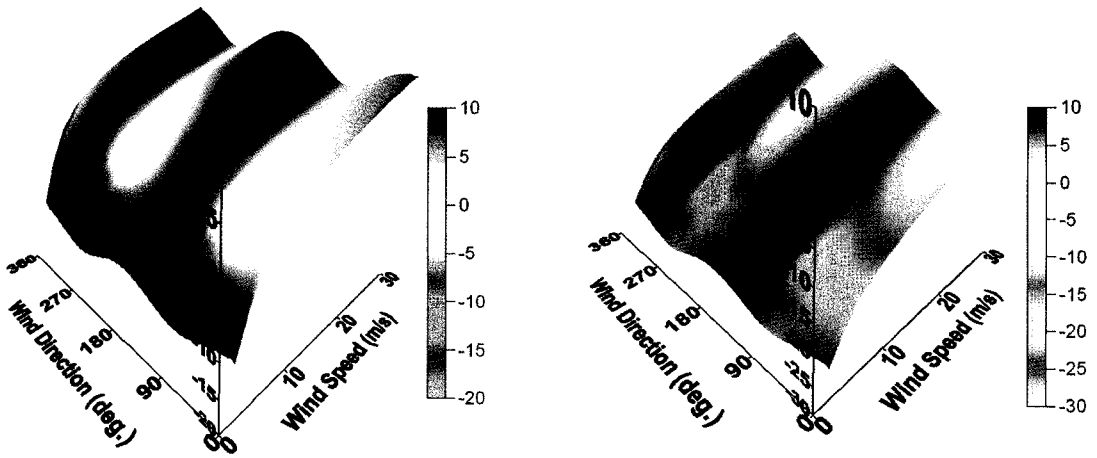

Fig. 3. Simulated X-band NRCS as a function of wind speed and wind direction for VV-polarization. (a) incidence angle of 25°; (b) incidence angle of 45°.

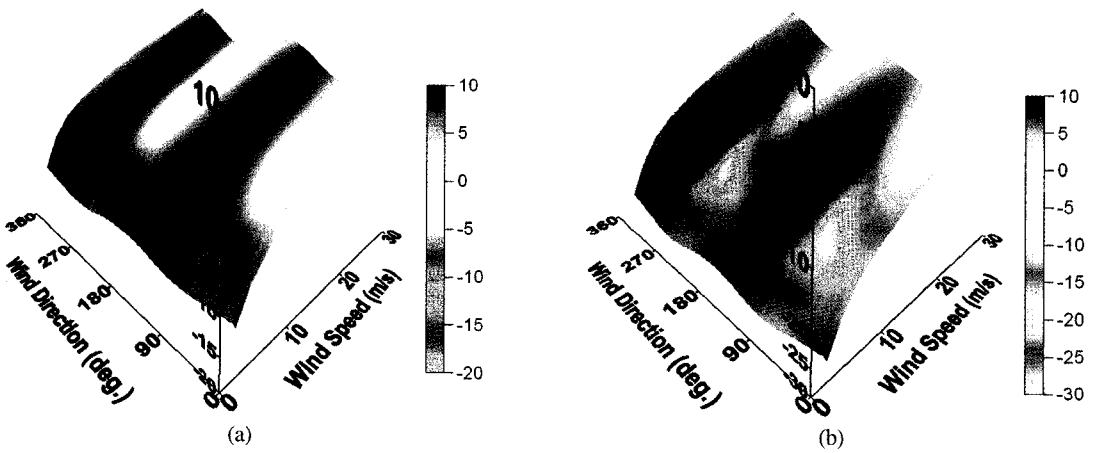

Fig. 4. CMOD4 NRCS as a function of wind speed and wind direction for VV-polarization. (a) incidence angle of 25°; (b) incidence angle of 45°.

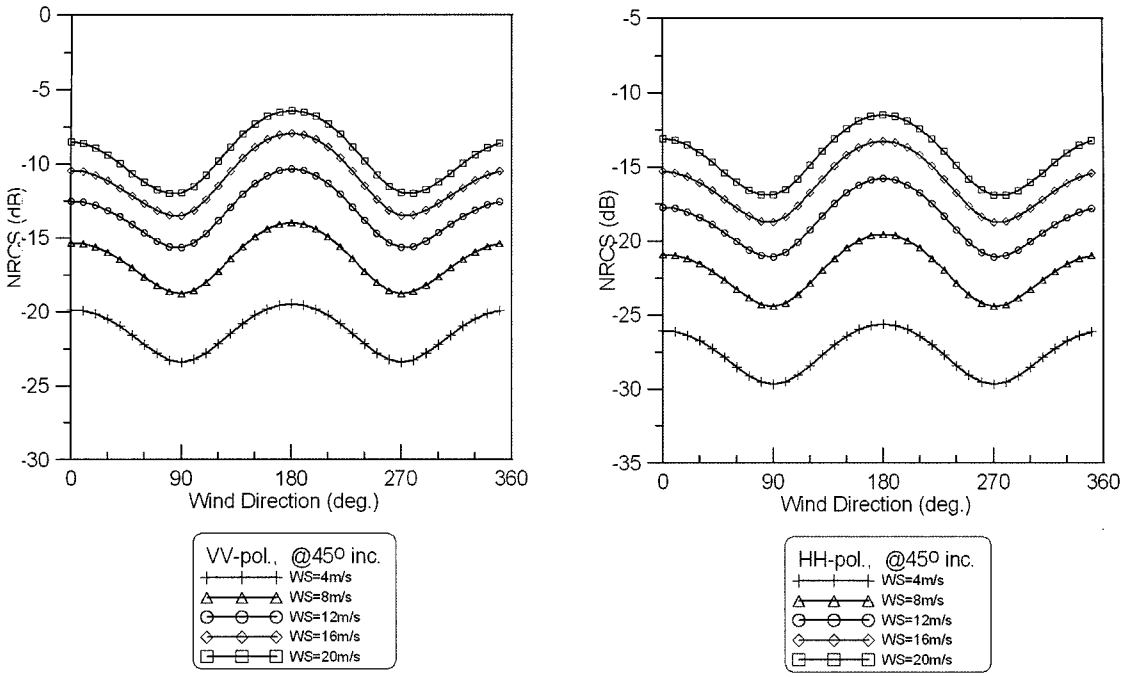

Fig. 5. Directional dependences of X-band NRCS at 45° incidence angle as simulated by the numerical models for wind speeds of 4, 8, 12, 16, and 20 m/s. (left) VV-polarization; (right) HH-polarization.

somewhat higher than the NRCS of CMOD4 at given wind speed and direction, and the sensitivity of X-band NRCS on wind speed is relatively higher at low wind speeds. This is because a higher radar frequency is more sensitive to shorter ocean surface waves, resulting in more sensitivity to wind variation at low winds. Fig. 5 shows the simulated X-band NRCS as a function of wind direction. One can observe the sinusoidal behaviour of the NRCS on the wind direction.

3. Wind Estimation from X-band SAR Data

Using the NRCS variation results as function of wind speed, direction and incidence angle, the sea surface wind was estimated from X-band SAR data. The X-band SAR data used in this study was TerraSAR-X which was made by DLR (German Aerospace Center). The TerraSAR-X data was collected in ScanSAR mode (Beam No. 8) on December 20th, 2007 at 09:28 (UTC), over the west coast of Korean peninsula. This data was acquired in VV-polarization and the surface coverage was approximately 100 km (range) by 150 km (azimuth) with 16 m spatial resolution.

The radiometric calibration process was performed to calculate the NRCS, which was required for wind speed estimation. Since TerraSAR-X data was processed and delivered in radar brightness (β_0), the NRCS (σ_0) could be calculated from the DN (digital number; amplitude of the SAR image) using the relationship (Fritz *et al.*, 2007):

$$\sigma_0 = \langle k_s \langle |DN|^2 \rangle - NEBN \rangle \sin(\theta) \qquad (16)$$

where θ is the local incidence angle, and k_s is a calibration and processor scaling factor (or calFactor), which are annotated in each product. NEBN (noise equivalent beta naught) could then be derived through

multiplying the same scaling factor to a noise profile that is also embedded on each product. The received data were the level 1b GEC (Geocoded Ellipsoid Corrected) product, which was multi-look detected and re-projected and re-sampled to the WGS84 reference ellipsoid. In the case of GEC products, they assumed an average height for the ellipsoid corrections; therefore the pixel location accuracy might vary from place to place depending on the terrain height. However, the ocean surface can easily be assumed as flat surface, and thus there were no significant distortions and differences in the ocean SAR image. However, because the images of GEC product had north up instead of heading up, a new mapping polynomial was generated to calculate incidence angles. The NRCS image calculated from the TerraSAR-X data is shown in Fig. 6.

The wind retrieval model was developed using the

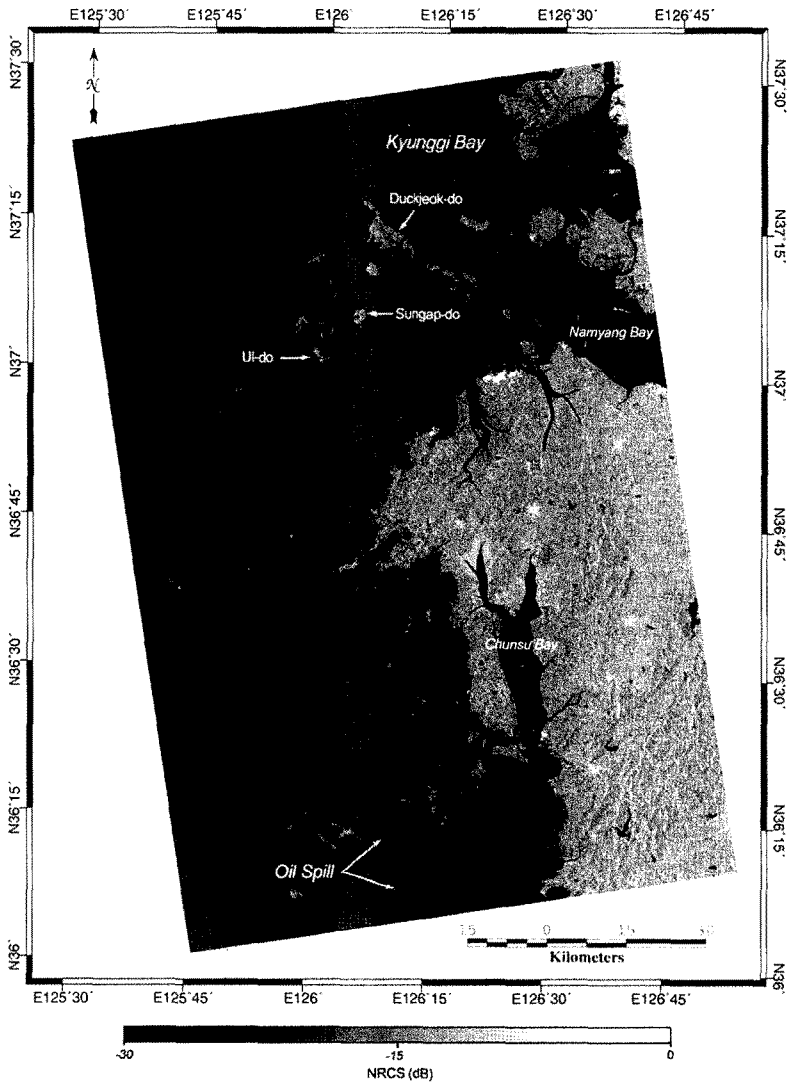

Fig. 6. NRCS image calculated from TerraSAR-X data obtained on December 20th, 2007, at 09:28 (UTC). The dark patches appeared in the southern part of the image were caused by oil spill of the Hebei Spirit accident in December 2007.

numerical model simulation results as functions of wind direction, wind speed, and incidence angle as explained in Section 2. The incidence angle values for GEC product were calculated in each pixel using the mapping polynomial as mentioned above. In general, the wind directions, which were required as input to the model, can usually be derived from wind aligned km-scale signatures in the SAR images such as wind streaks and atmospheric roll vortex, or from the imprint of the island's lee shadow. However, these signatures were not observed in the TerraSAR-X image as many as needed. Thus, the wind directions measured from the automatic weather station (AWS) at the time of SAR data acquisition were used in this study (Fig. 7). These wind directions were then interpolated to whole image area using kriging method. For the kriging interpolation scheme, exponential semivariogram model was used, and the values of the range and nugget were 500 and 0.01, respectively. The interpolations were performed both in east-west and north-south components of wind direction. One can observe the interpolated wind directions agree well with the imprints of the island's lee which can be seen around Duckjeok

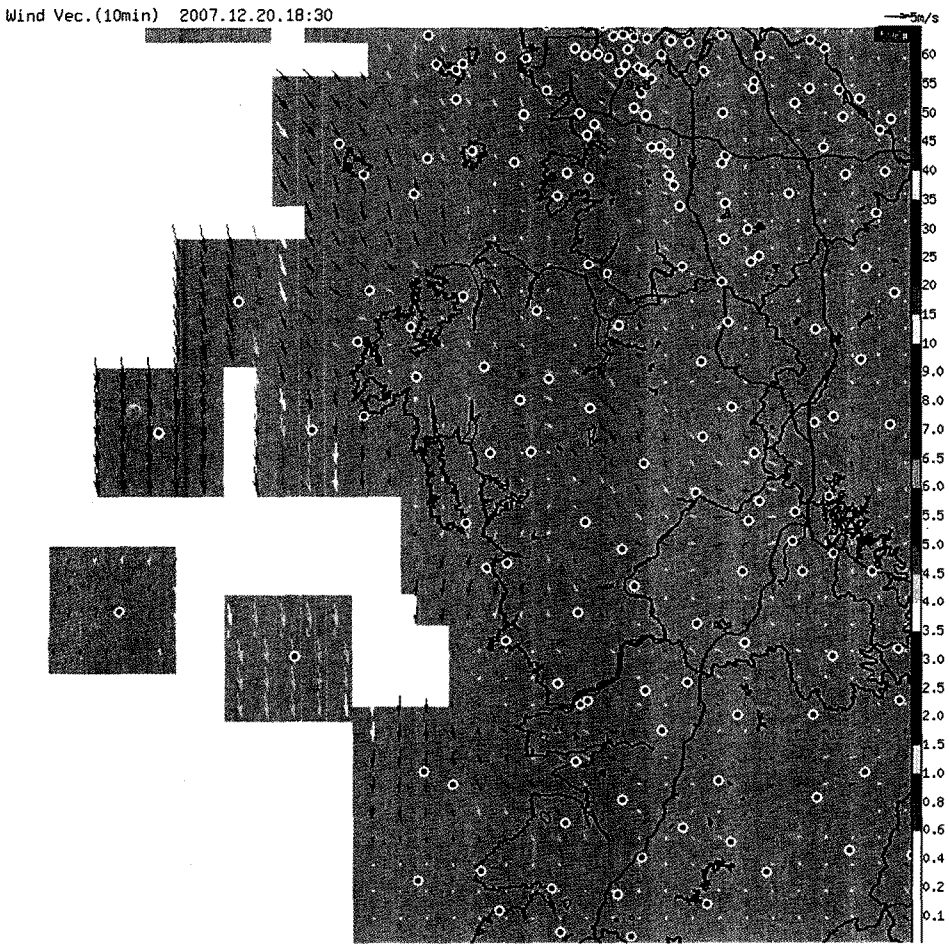

Fig. 7. Wind vectors generated from Automatic Weather Stations (AWSs) around the study area (http://www.kma.go.kr). The locations of AWS were plotted in red circles. The local time of TerraSAR-X acquisition was at 18:28 (LT) on December 20th, 2007.

Islands such as Sungap-do and Ul-do in Fig. 6. The resulting wind speeds estimated from TerraSAR-X were displayed in Fig. 8. The estimated wind speeds appear to agree fairly well with the AWS measurements. The relatively low wind speeds were estimated in Kyunggi Bay, Namyang Bay, and Chunsu Bay, and the similar wind speeds were also observed by AWSs of those areas.

4. Conclusion and Discussion

Currently several X-band SAR systems have been developed and are operating. Korea is also planning to launch the nation's first high resolution X-band SAR satellite (KOMPSAT-5) in 2010. Thus, it is timely and necessary to develop X-band GMF for extracting high resolution wind field from these

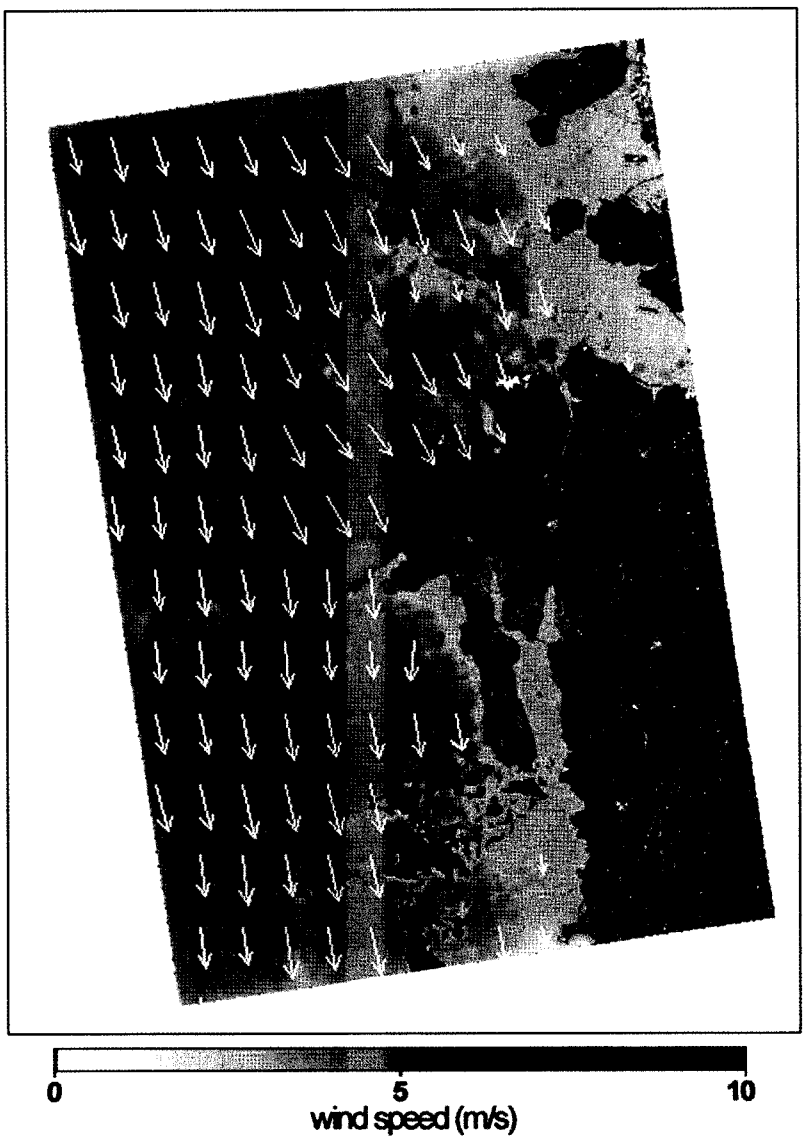

Fig. 8. Wind field estimated from TerraSAR-X data. The oil spilled area was masked out in this analysis.

emerging X-band SAR systems. In this study, X-band wind retrieval model was developed based on theoretical models (radar backscattering model and hydrodynamic interaction model). Even though these models were physically based and assumed the equilibrium state of ocean surface wave, the model simulation results showed the explicit dependence of wind speed and direction in X-band and reasonably well estimated wind speeds from TerraSAR-X data acquired in the west coast of Korean peninsula.

As the in-situ measurements of NRCS increase, the X-band wind retrieval model can be improved to increase the accuracy of the wind speed estimates. The equilibrium ocean wave spectrum can be further tuned and optimised with these in-situ measurements. It is strongly required to collect well-calibrated NRCS values using ground based scatterometers or X-band SAR data over the ocean as many as possible.

Acknowledgements

This work was funded by the Korea Meteorological Administration Research and Development Program under Grant CATER 2009- 3113. The TerraSAR-X data used in this study was provided by the DLR (German Aerospace Center) through the Announcement of Opportunity with Younsoo Kim (PI) (#LAN0174).

References

Elfouhaily, T., B. Chapron, K. Katsaros, and D. Vandemark, 1997. A unified directional spectrum for long and short wind-driven waves, *Journal of Geophysical Research*, 102: 15-15.

Fritz, T., M. Eineder, M. Lachaise, A. Roth, H. Breit, B. Schattler, and M. Huber. 2007. TerraSAR-X Ground Segment Level 1b Product Format Specification: TX-GS-DD-3307.

Hersbach, H., A. Stoffelen, and S. De Haan, 2007. An improved C-band scatterometer ocean geophysical model function: CMOD5, *Journal of Geophysical Research*, 112(C3): C03006, doi:03010.01029/02006JC003743.

Hughes, B., 1978. The effect of internal waves on surface wind waves 2. Theoretical analysis, *Journal of Geophysical Research*, 83(C1): 455-465.

Komen, G. 1994. *Dynamics and modelling of ocean waves*: Cambridge University Press.

Lehner, S., J. Schulz-Stellenfleth, S. Brusch, and M. Eineder, 2007. Validation of an X-band SAR wind algorithm by SIR-C/X SAR data, *IGARSS* 2007.

Lyzenga, D. and J. Bennett, 1988. Full-spectrum modeling of synthetic aperture radar internal wave signatures, *Journal of Geophysical Research*, 93: 12345-12354.

Masuko, H., K. OKAMOTO, M. Shimada, and S. Niwa, 1986. Measurement of microwave backscattering signatures of the ocean surface using X band and K (a) band airborne scatterometers, *Journal of Geophysical Research*, 91(C11): 13065-13083.

Phillips, O., 1977. *The dynamics of the upper ocean.* New York: Cambridge University Press.

Plant, W., 1982. A relationship between wind stress and wave slope, *Journal of Geophysical Research*, 87(C3): 1961-1967.

Romeiser, R., W. Alpers, and V. Wismann, 1997. An improved composite surface model for the radar backscattering cross section of the ocean surface, 1. Theory of the model and optimization/validation by scatterometer data, *Journal of Geophyscial Research*, 102:

25237-25250.

Stoffelen, A. and D. Anderson, 1997. Scatterometer data interpretation: Estimation and validation of the transfer function CMOD4, *Journal of Geophysical Research*, 102(C3): 5767-5780.

Thompson, D. and R. Gasparovic, 1986. Intensity modulation in SAR images of internal waves, *Nature*, 320: 345-348.

Thompson, D., F. Monaldo, J. Horstmann, and M. Christiansen, 2008. Geophysical model functions for the retrieval of ocean surface winds, *SEASAR 2008*.

Valenzuela, G., 1978. Theories for the interaction of electromagnetic and oceanic waves - A review, *Boundary-Layer Meteorology*, 13(1): 61-85.

Wright, J., 1968. A new model for sea clutter, *IEEE Transactions on Antennas and Propagation*, 16(2): 217-223.